

pubs.acs.org/JACS Article

Electrosynthesis of Agrochemicals via Alternating-Current-Driven Selective, Continuous Dehalogenation

Diptangshu Datta Mal, Nikita Redkar, Kaida Liu, Hyoju Park, Ellis Rae Kennedy, Sungin Kim, Wenqi Li, Yao Yang,* Yue Qi,* Matthew Neurock,* and Long Luo*



Cite This: https://doi.org/10.1021/jacs.5c12620



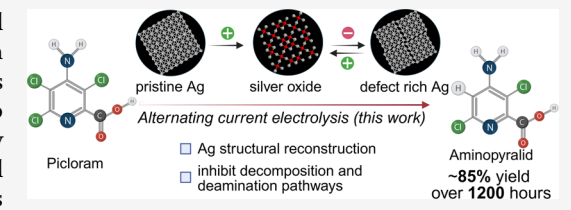
ACCESS I

III Metrics & More

Article Recommendations

s Supporting Information

ABSTRACT: Dehalogenation is a critical transformation in chemical synthesis but remains limited by catalyst deactivation and low selectivity in industrial processes. Here, we report an alternating current (AC) electrolysis strategy for the selective, continuous dechlorination of picloram to aminopyralid, a widely used herbicide. Conventional electrolysis, currently used in industrial aminopyralid electrosynthesis, suffers from structural degradation of the Ag catalyst and the in situ formation of reactive species (ClO $^-$, NH $_3$, and NO $_2^-$), leading to reduced product yields (<30%) and



increased side-product formation. By contrast, AC electrolysis sustains catalytically active, defect-rich Ag surfaces through periodic redox cycling and minimizes the accumulation of ClO^- and NO_2^- , thereby suppressing side reactions. The optimized AC protocol achieves a yield of >85% aminopyralid with >90% conversion, enabling uninterrupted operation in a flow system for over 50 days. This work not only advances the industrial electrosynthesis of aminopyralid but also highlights AC electrolysis as a broadly applicable platform for enhancing selectivity and catalyst durability in electrocatalytic transformations.

■ INTRODUCTION

Dehalogenation is a cornerstone transformation in organic synthesis, playing a vital role in the production, modification, and detoxification of halogen-containing compounds across diverse industrial sectors, including agrochemicals, pharmaceuticals, polymers, and environmental remediation technologies (Figure 1a and Tables S1 and S2).1-7 For example, it is essential in the manufacture of vinyl chloride—the monomer for polyvinyl chloride, which commands a global market exceeding \$90 billion and hydrocortisone, to a widely used corticosteroid pharmaceutical with a market value of \$1.25 billion. 11 In the agrochemical sector, dehalogenation is also critical for the synthesis of widely adopted herbicides and pesticides, such as aminopyralid, 2-methyl-4-chlorophenoxyacetic acid, and clopyralid, which span a market range of \$1.2-1.8 billion. 12,13 Beyond synthetic applications, dehalogenation has gained increasing importance in mitigating persistent environmental organic pollutants, including polychlorinated biphenyls and chlorofluorocarbons. 14-16

Despite the significance of dehalogenation in industrial applications, current methodologies continue to face critical challenges, including catalyst deactivation, low product selectivity, and limited operational stability. These limitations hinder their long-term viability in industrial settings. A summary of a few selected industrial dehalogenation processes and their performance metrics is provided in Table S3. 17,18

A representative example is the synthesis of aminopyralid (2) via electrochemical dechlorination of picloram (1). Both 1 and 2 are commercially available herbicides. 2 was introduced

by Dow AgroSciences in 2005 as a safer and more selective alternative to 1, offering lower soil mobility and reduced environmental toxicity. ^{19,20} As of 2023–2024, global production of 2 is estimated at 0.5 million lbs annually, with a global market value of around \$1.5 billion (Figure 1b). ^{21,22} Industrial synthesis relies on the electrochemical dehalogenation of 1 using an Ag cathode in an aqueous NaOH/NaCl solution, operated under constant potential conditions. ^{23,24} The Ag cathode is anodically activated (oxidized and then reduced) prior to use (see Supporting Information for details). Despite full conversion of 1, the yield of 2 is limited to around 26%, as disclosed in the original patent (Figure 1c). ^{23,24} Moreover, the reaction mechanism remains poorly understood, and no definitive solution has been established.

In this work, we developed an alternating current (AC) electrolysis strategy to address the challenges of product selectivity and catalyst deactivation during the electrolysis of 1 (Figure 1e). This AC electrolysis method sustains catalytically active, defect-rich Ag surfaces through periodic redox cycling while minimizing the accumulation of ClO⁻ and NO₂⁻, thereby suppressing undesired side reactions. The optimized AC protocol achieves a yield of over 85% with a conversion

Received: July 23, 2025
Revised: September 19, 2025
Accepted: September 22, 2025



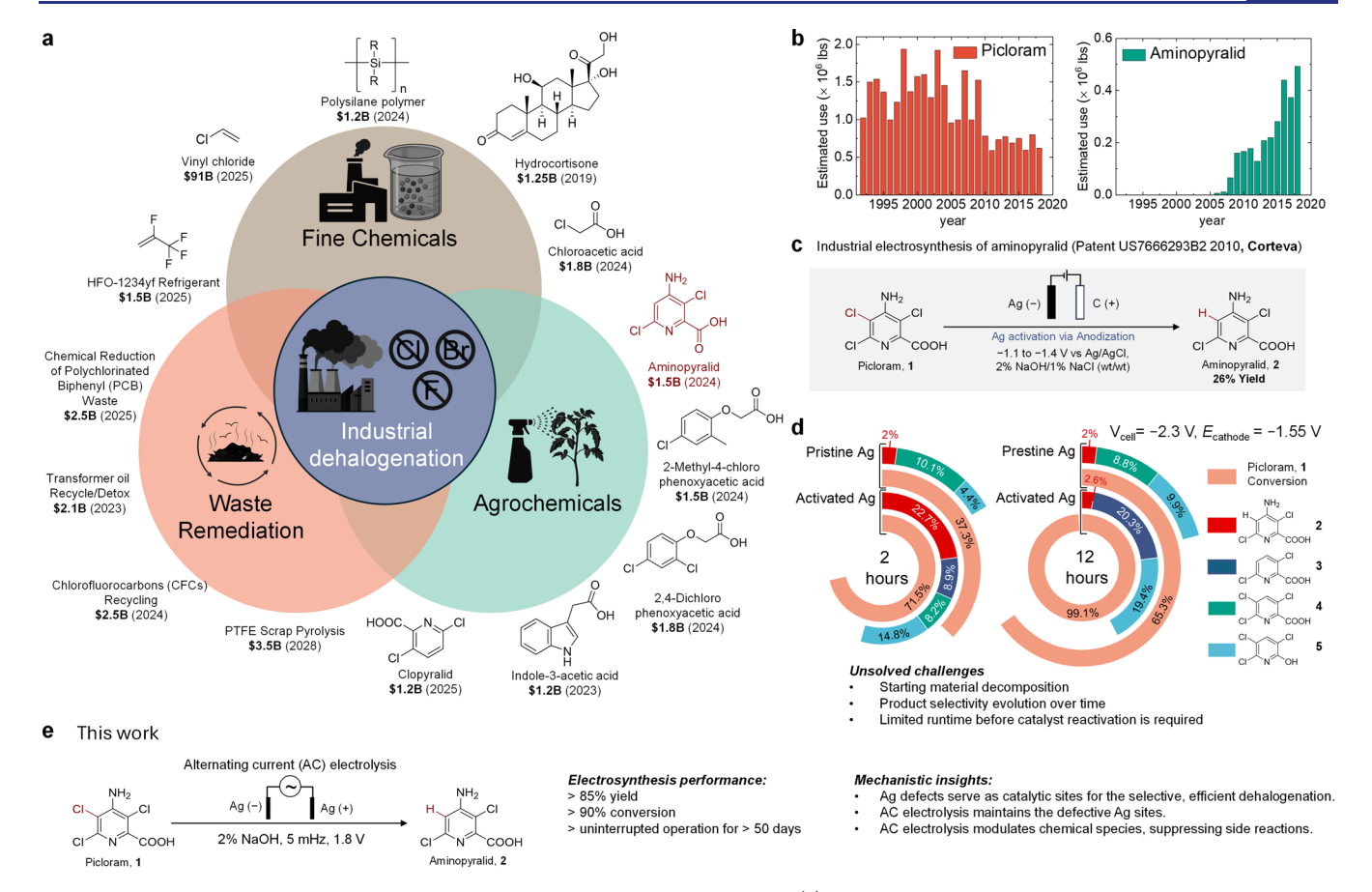


Figure 1. Importance and challenges of dehalogenation in the chemical industry. (a) Schematic illustration of major industrial products that depend on dehalogenation reactions, with a total approximate market value of \sim \$115B. Icons were created with BioRender. (b) Annual consumption trends of the herbicides picloram (1) and aminopyralid (2). (c) Industrial electrosynthesis of 2 by electrochemical dechlorination of 1, based on US7666293B2 (2010, Corteva). (d) Comparison of reaction performance after 2 and 12 h using pristine and anodically activated Ag electrodes under the industrial electrolysis conditions disclosed in the patent. The side panel shows the molecular structures of the main and side products. Electrolysis conditions: Ag rod cathode and graphite plate anode; cell voltage (cathode vs anode) = -2.3 V; electrolyte: 2 wt % NaOH/1 wt % NaCl in water; initial [1] = 32 mM. (e) The alternating current (AC) electrolysis strategy developed in this work addresses the challenges of product selectivity and catalyst deactivation during the electrolysis of compound 1.

rate of over 90%, enabling uninterrupted operation in a flow system for more than 50 days. This innovation is based on our fundamental understanding of the underlying reaction mechanisms, which are described in detail below.

■ RESULTS AND DISCUSSION

Mechanistic Insights into the Industrial Process for Aminopyralid Electrosynthesis. We first coupled catalyst characterization, electrochemical kinetic studies, and theory to elucidate the mechanism for the industrial electrosynthesis of 2 from 1. We reproduced the reaction on a laboratory scale following the original patent.²⁴ The setup included an Ag rod as the cathode and a graphite plate as the anode in a twoelectrode configuration (Figure S1). The electrolyte was composed of 2 wt % NaOH and 1 wt % NaCl in water, and a cell voltage of -2.3 V was applied, corresponding to a cathode potential of approximately -1.55 V vs Ag/AgCl. The reaction was performed using both pristine and anodically activated Ag electrodes to evaluate the effect of anodic activation—a critical step used in production.²⁴ Pristine Ag is a mechanically polished metal rod electrode. The activated Ag was prepared by applying a +2.3 V voltage bias for 300 s, followed by a reversed voltage of -2.3 V for the remainder of the reaction. After 2 h, product analysis revealed an

enhancement in catalytic activity following electrode activation. With activated Ag, 71.5% of substrate 1 was converted, yielding 22.7% of product 2, which is comparable to the industrial process (\sim 26%), whereas pristine Ag resulted in only 37.3% conversion and a substantially lower 2 yield. However, after 12 h, both Ag electrodes only produced ~2% of 2 and a poor mass balance, suggesting extensive degradation of both the starting material and the desired product. Several deaminated byproducts were identified, including clopyralid (3), 3,5,6-trichloropicolinic acid (4), and 3,5,6-trichloro-2pyridinol (5)—all structurally derived from either 1 or 2, causing a major decrease in the yield of 2. These results demonstrate that, while anodic activation of the Ag electrode substantially boosts initial reactivity, prolonged electrolysis under constant potential conditions leads to Ag deactivation, diminished selectivity, and increased formation of undesired deaminated products.

To understand the impact of anodic activation and the subsequent loss of reactivity over time, we characterized the structural and electrocatalytic evolution of the Ag electrode throughout the activation process and extended electrolysis. Scanning electron microscopy (SEM) images (Figure S19) reveal distinct microscale morphological transitions: the initially smooth, flat surface of pristine Ag develops spherical

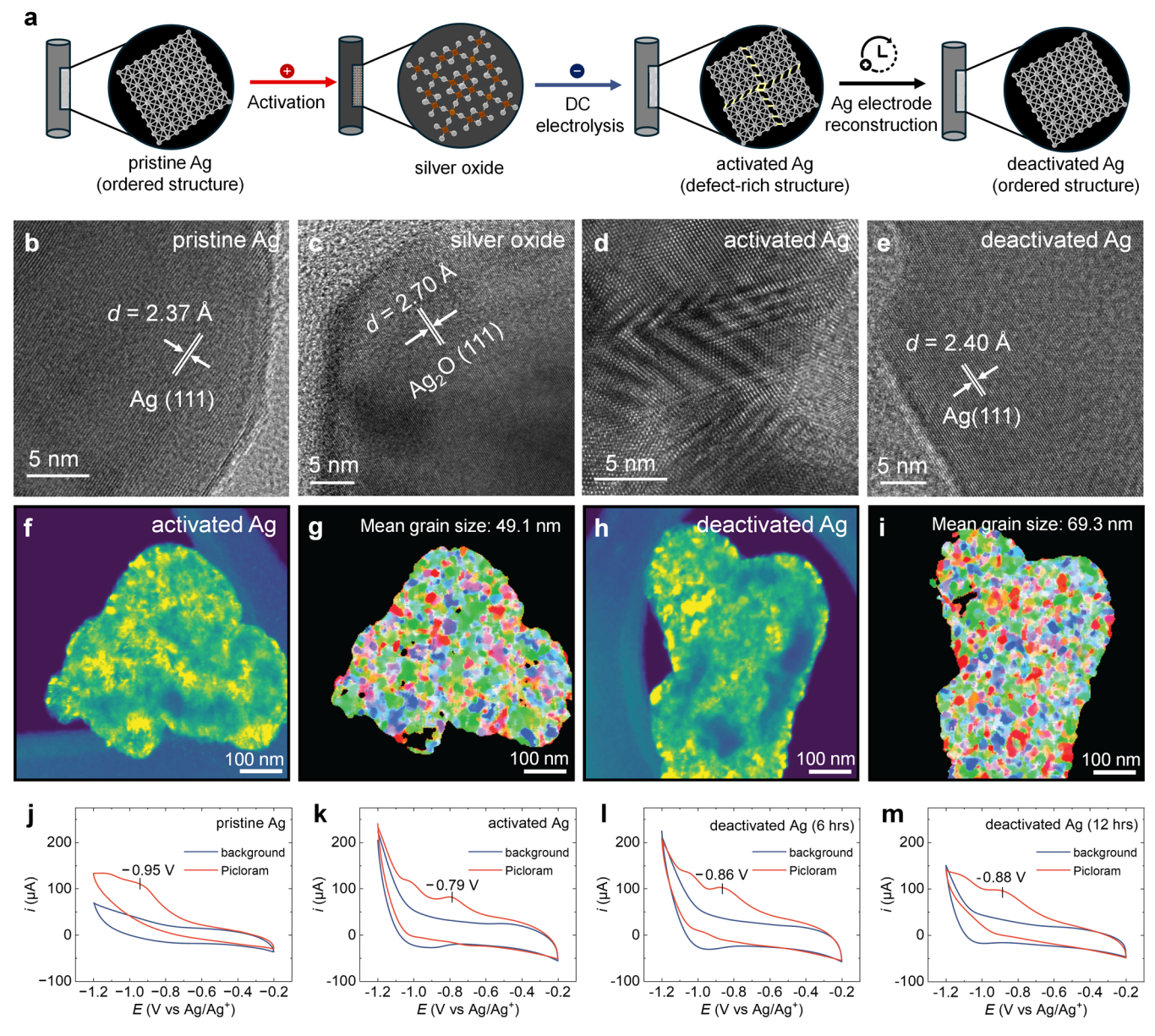


Figure 2. Structural and activity evolution of the Ag catalyst during the electrosynthesis of 2. (a) A schematic illustration of the anodic activation of Ag and its deactivation during prolonged electrolysis. The defects formed by the reduction of Ag_2O through negative pulse are highlighted in yellow. (b–e) TEM images highlight structural features, including ordered Ag (111) planes in pristine Ag, Ag_2O (111) planes in Ag_2O , defect-rich features in activated Ag, and partial recovery of the ordered structure in deactivated Ag. (f, h) Representative virtual ADF-STEM images with regions of high intensity (yellow) corresponding to on-zone electron diffraction within the virtual detector range, and (g, i) 4D-STEM grain maps of activated Ag and deactivated Ag highlighting the density of grains within the particles and mean grain sizes. (j–m) CVs using 1 as the substrate demonstrate shifts in reduction potential depending on the state of the Ag catalyst. Electrolyte: 0.05 M tetrabutylammonium perchlorate (TBAP) in acetonitrile; 8 mM picloram; scan rate: 0.05 V/s; working electrode: 3 mm Ag disk; counter electrode: Pt wire; reference electrode: nonaqueous Ag/5 mM Ag^+ in acetonitrile with 0.05 M TBAP.

features after anodic treatment. These features become finer and porous upon reduction during potential bias reversal (i.e., anodically activated Ag) and eventually evolve into flake-like structures following 12 h of electrolysis (deactivated Ag). Transmission electron microscopy (TEM) images (Figure 2b–e) further distinguish structural differences among the samples. Pristine and deactivated Ag both exhibit ordered Ag(111) lattice fringes, whereas activated Ag displays pronounced disorientation and defect sites. These defects result from structural collapse associated with the reduction of Ag₂O, formed during anodic activation. This phenomenon is similar to one observed in other oxide-derived metallic catalytic

materials. $^{25-27}$ Despite these morphological differences, time-dependent XRD results in Figure S17 show that Ag₂O formed during the anodic pulse was completely converted to metallic Ag within 20 s. This suggests that the active catalyst should be metallic Ag, not Ag oxides, in activated Ag and deactivated Ag samples.

Virtual annular dark-field (ADF) STEM images reveal that both activated and deactivated Ag grains display high densities of individual crystalline Ag grains (Figure 2f,h). In addition, four-dimensional scanning transmission electron microscopy (4D-STEM) measurements were used to rapidly record a 2D diffraction pattern (crystallographic analysis) in reciprocal

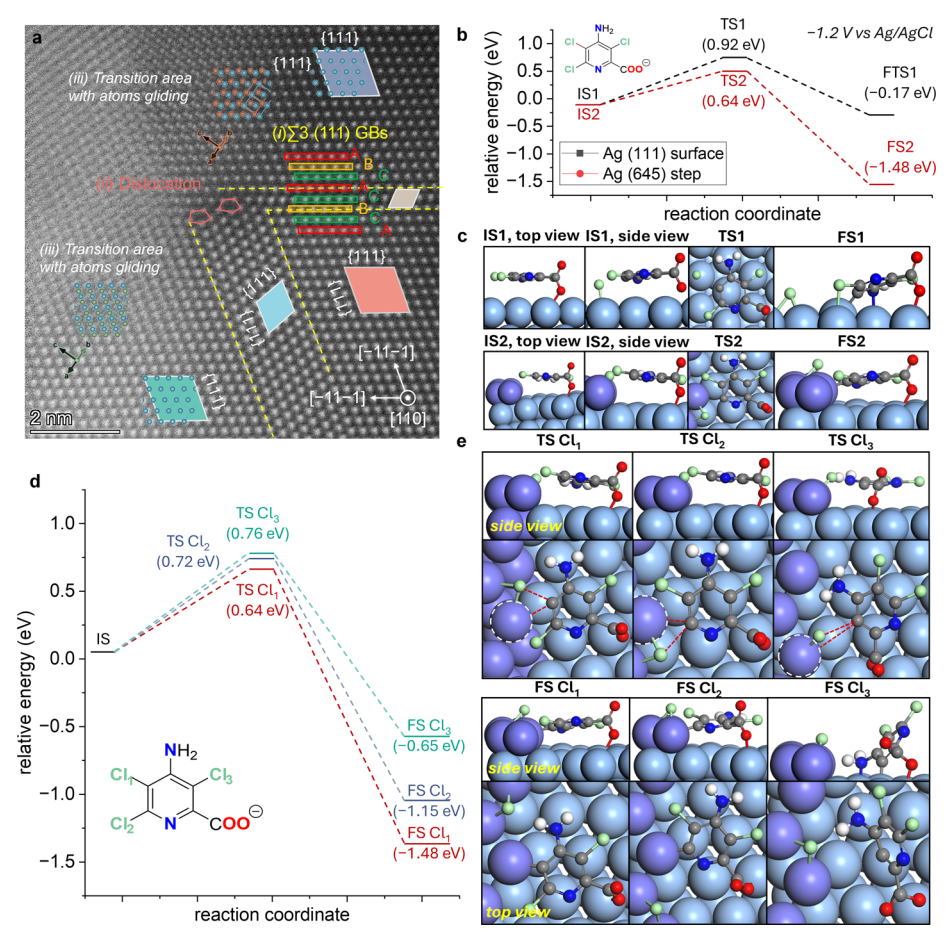


Figure 3. Roles of Ag defect sites in the selective dechlorination of 1. (a) High-resolution STEM image of activated Ag showing different types of defects. (b) Energy profiles and (c) binding geometries during electrocatalytic dechlorination of 1 to form 2, showing a lowered transition state (TS) energy on the Ag(645) step surface with undercoordinated step sites compared to an ordered Ag(111) surface. (d) Energy profiles and (e) TS binding geometries for breaking different C–Cl bonds of substrate 1. The positioning of the stabilizing Na⁺ cations is shown in Figure S23.

space as the electron beam scans over every pixel of the 2D image (atomic positions) in real space. ^{28,29} 4D-STEM, based on an electron microscopy pixel array detector (EMPAD), ³⁰ can identify individual crystalline grains with various orientations (different colors) within the activated and deactivated Ag nanoparticles (Figure 2g,i). 4D-STEM grain maps reveal that the deactivated Ag consists of larger crystal grains (69.3 nm) compared to activated Ag (49.1 nm). This indicates that activated Ag grains experienced mild particle aggregation, leading to a decrease in the density of active sites. Details of 4D-STEM analysis can be found in Figures S20 and S21.

Having established the structural evolution of the Ag electrode, we next examined how these changes influence the electrochemical reduction of 1. Cyclic voltammetry (CV) was conducted in acetonitrile to avoid interference from the hydrogen evolution reaction common in aqueous media (Figure S33). On pristine Ag, the reduction peak for 1 was observed at -0.95 V vs Ag/Ag $^+$ (Figure 2j). After anodic activation, the peak shifted positively to -0.79 V (Figure 2k), indicating enhanced catalytic activity toward dehalogenation. However, following 6 h of electrolysis, the peak potential shifted back to -0.86 V, and further to -0.88 V after 12 h (Figure 2l-m), reflecting a progressive decline in catalytic performance. These electrochemical results are consistent with the structural degradation of activated Ag, as shown in Figure

2f–i, and the corresponding synthetic outcomes in Figure 1d. We also performed CVs of all products (2, 3, 4, and 5) under the same conditions as those for substrate 1 (Figure S34). We found that all exhibited similar reduction potentials, with a reduction peak potentials in the narrow range of -0.85 to -1.0 V vs Ag/Ag⁺.

These findings support a proposed mechanism for the activation and subsequent deactivation of the Ag electrode during the industrial electrosynthesis of **2**, as illustrated in Figure 2a. During anodic activation, a positive voltage pulse first oxidizes Ag to form Ag₂O. A subsequent negative pulse reduces Ag₂O back to Ag, removing lattice oxygen and creating many high-energy defect sites that act as catalytic centers. ^{31–33} However, these defect-rich structures are unstable and gradually revert to the lower-energy, less active deactivated form over time, accompanied by an increase in grain size. ^{32,34} As a result, the catalytic activity decreases, and the structure returns to one similar to the original silver.

Origin and Loss of Product Selectivity. To understand how the defective structure of activated Ag influences the reaction selectivity, we performed high-resolution STEM characterization. As shown in Figure 3a, activated Ag exhibits a range of structural defects, including: (i) multiple $\Sigma 3(111)$ grain boundaries with the characteristic ABC stacking sequence of fcc Ag; (ii) dislocations located at the convergence points of $\Sigma 3(111)$ grain boundaries; and (iii) atomic gliding,

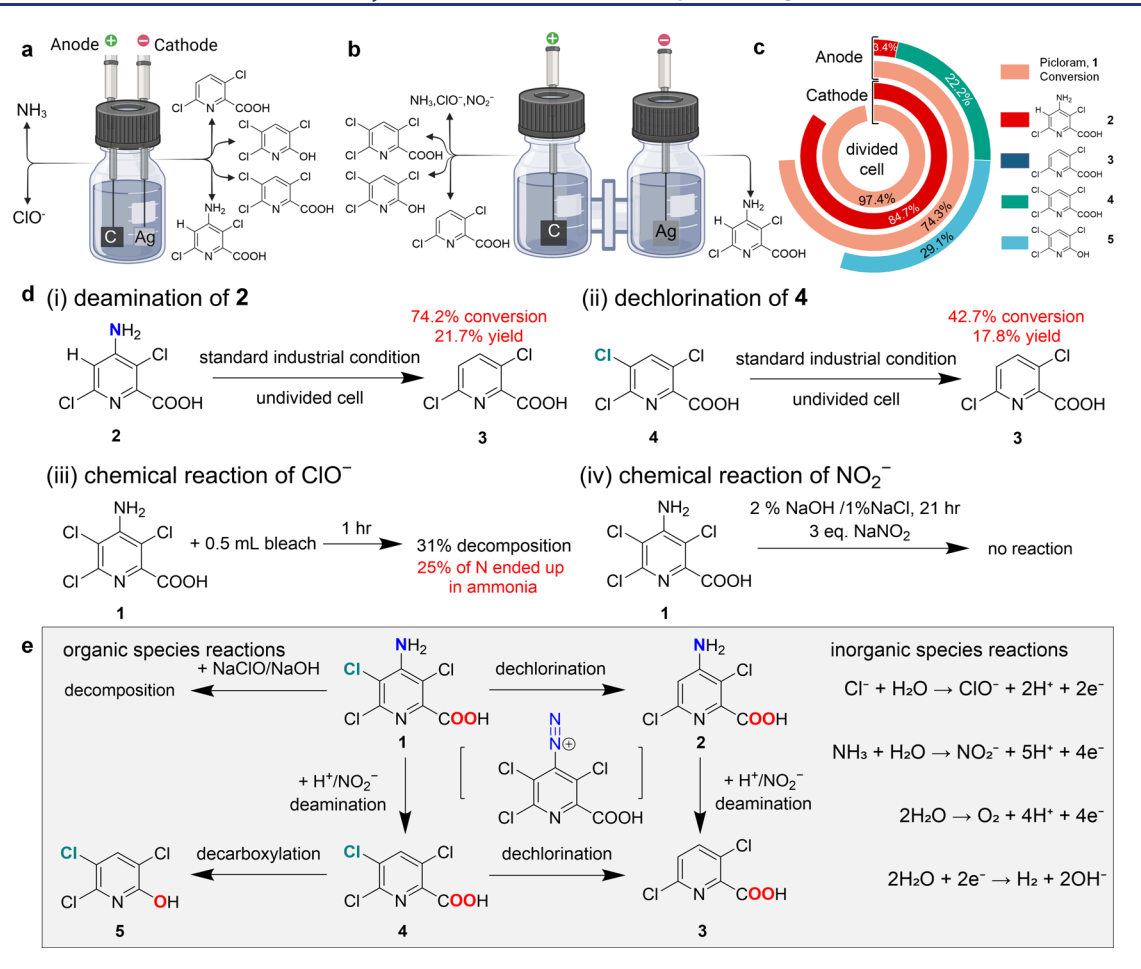


Figure 4. Chemical species identification and their roles in controlling product selectivity during electrosynthesis of 2. (a, b) Products identified in (a) an undivided cell and (b) a divided cell under standard electrosynthesis conditions. Electrochemical cell elements were created with BioRender. (c) Conversion of 1 and product yields on the cathodic and anodic sides of the divided cell. (d) Control experiments elucidating the interconversion between the major inorganic and organic species during electrosynthesis. (e) Proposed reaction pathways governing the formation of 2 and side-product distribution under standard electrolysis conditions.

observed from the [110] zone axis. The frequency of these defects significantly decreased in the deactivated Ag nanoparticles (Figure S18), which is consistent with their average larger grain size in 4D-STEM analysis (Figure 2i).

Due to the structural complexity of activated Ag, modeling its defective features directly is challenging. Herein, we used the Ag(645) surface, which exposes step edges along Ag(111) slip planes and presents terrace, step edges, and corner sites with metal coordination numbers of 9, 8, and 6, respectively. Potential-dependent density functional theory (DFT) calculations using an implicit aqueous solvent were carried out to examine the reaction energies and activation barriers for C–Cl bond activation at the coordinatively unsaturated sites on the Ag(645) surfaces and the coordinatively saturated sites of flat Ag(111), which represents the pristine Ag surface for comparison. Computational details are provided in the Supporting Information.

The reaction proceeds via the insertion of an Ag atom into the C–Cl bond. The reaction energy profiles for the C–Cl₁, -Cl₂, and -Cl₃ bond activation shown in Figure 3b reveal distinct reactivity trends resulting from differences in surface atom coordination. The activation of the C–Cl₁ bond of 1 at the operating conditions of -1.2 V Ag/AgCl on the Ag(111) surface exhibits a high activation barrier (0.92 eV) and a modestly exergonic reaction energy (-0.17 eV), due to limited

stabilization of the activated chlorine and carbon species. In contrast, the Ag(645) surface more effectively stabilizes these intermediates, resulting in a substantially lower activation barrier for $C-Cl_1$ activation (0.64 eV) and a significantly higher exergonic reaction energy (-1.48 eV). These findings are corroborated by the transition state (TS) and final state (FS) structures shown in Figure 3c, where intermediates exhibit enhanced interactions with the under-coordinated edge sites on Ag(645), facilitating a more favorable reaction pathway.

To elucidate the site-selective dechlorination on the Ag(645) surface, we computed reaction energy profiles for the cleavage of three different C–Cl bonds (Cl_1 , Cl_2 , and Cl_3). As shown in Figure 3d, the C– Cl_1 bond cleavage exhibits the lowest activation barrier (0.64 eV) and the most favorable reaction energy (-1.48 eV), indicating that Cl_1 is the most reactive site. In contrast, C– Cl_3 bond cleavage has the highest barrier (0.76 eV) and the least favorable thermodynamics (-0.65 eV). This diminished reactivity can be attributed to the steric hindrance imposed by the neighboring bulky carboxylate ($-COO^-$) and amino ($-NH_2$) groups. Upon C– Cl_3 bond scission, the resulting carbon-centered radical is spatially constrained and unable to approach the low-coordinated edge sites of the Ag (645) surface. As a result, it remains adsorbed on the terrace region, which offers weaker

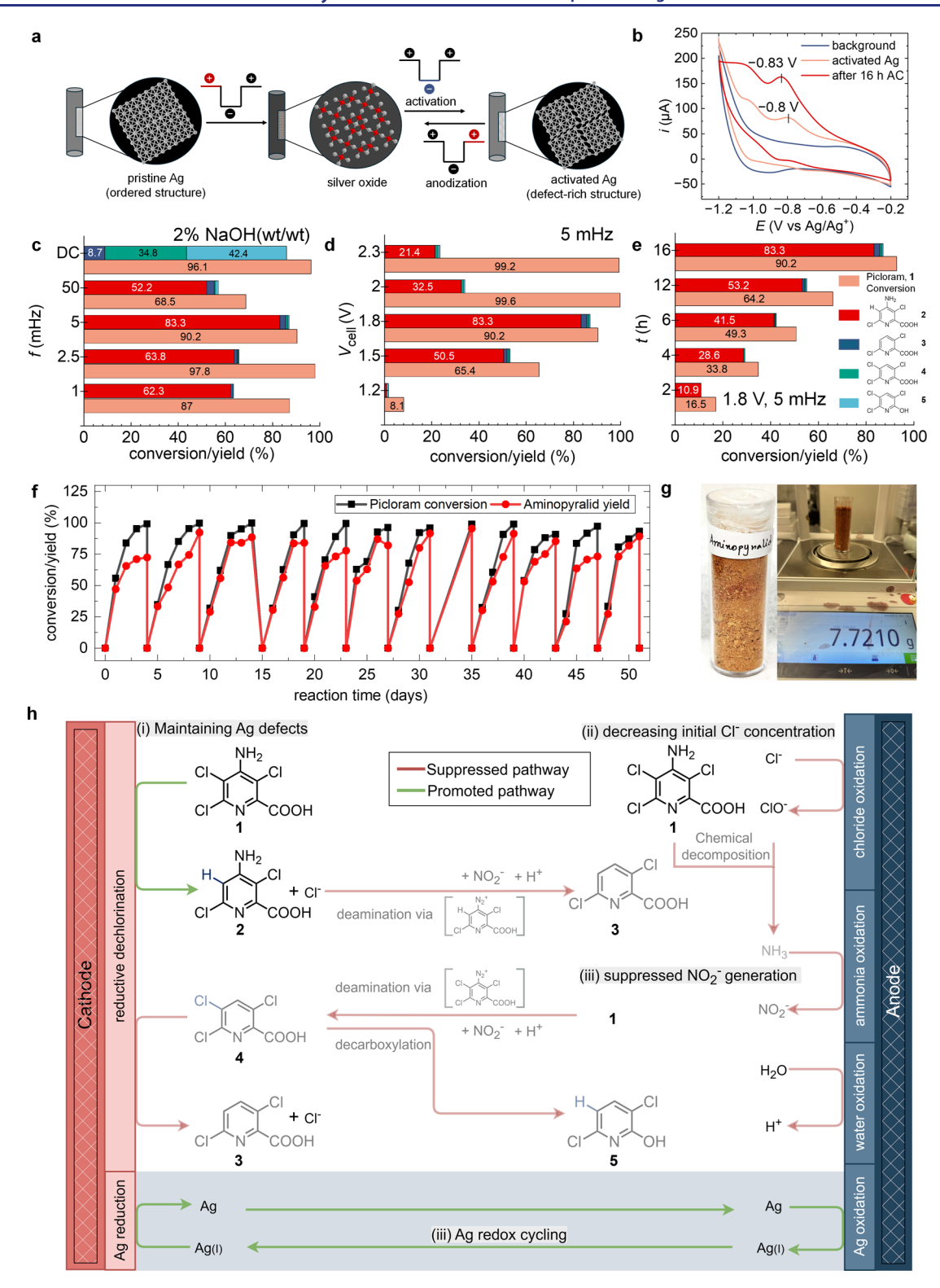


Figure 5. Selective and continuous electrosynthesis of 2 under AC electrolysis. (a) Proposed continuous regeneration of defective Ag under AC electrolysis to prevent catalyst deactivation and sustain high activity over extended reaction times. (b) CVs of 8 mM 1 in acetonitrile with 0.05 M TBAP, using freshly activated Ag and Ag after 16 h of AC electrolysis under optimal conditions (frequency = 5 mHz, amplitude = 1.8 V). Scan rate: 0.05 V/s; working electrode: 3 mm Ag disk; reference electrode: Ag/5 mM Ag⁺. (c, d) Optimization of AC electrolysis conditions with respect to (c) frequency and (d) voltage amplitude. Electrolyte: 2 wt % NaOH in water; reaction time: 16 h. Results from industrial electrolysis conditions (voltage bias = -2.3 V for 12 h), labeled as DC, are included for comparison. (e) Time-dependent conversion of 1 and yield of 2 under optimal AC conditions (two Ag rods as electrodes, 2 wt % NaOH, initial [1] = 32 mM, 1.8 V, 5 mHz). (f) Conversion of 1 and yield of 2 across 12 consecutive 1 g scale batches over 50 days of continuous AC electrolysis in a flow cell without reactivating the Ag catalyst. (g) Photograph of isolated product 2 after simple workup of the continuous-flow reaction mixture. (h) Proposed mechanism for AC-driven selective electrosynthesis of 2.

stabilization and thus a less favorable energetic pathway (Figure 3e).

The higher selectivity for Cl₁ dechlorination over Cl₂ on the Ag(645) surface is attributed to a combination of electronic and geometric factors that stabilize or destabilize their TS. Cl₁ is positioned adjacent to an NH2 group, which is a strong electron-donating substituent that hinders direct $C-C_1$ dechlorination in solution. Upon the adsorption of 1 on the Ag(645) surface, the nitrogen of the NH₂ group is oriented directly above an Ag site in the lower Ag terrace (Figures S25a and S27a), thus allowing for direct electron transfer from NH₂ to Ag, which enhances the reductive C-Cl₁ activation. Cl₂, on the other hand, is positioned as an adjunct to the pyridinic N. As the ring sits parallel to the lower Ag terrace, there is charge transfer from the metal to the pyridinic N (Figures S25c and S27c), thus minimizing its ability to aid in inductive C-Cl₂ activation. Taken together, these substituent and geometric effects render Cl₁ dechlorination both kinetically and thermodynamically more favorable than Cl₂ on the Ag(645) surface. Collectively, these results indicate the crucial role of zig-zag Ag edge sites in promoting selective dechlorination at the C₁ position of 1, thereby facilitating efficient formation of

After establishing through theoretical modeling that the C– Cl_1 bond undergoes preferential cleavage on the activated Ag surface, a critical question remains: how are the other major side-products (3, 4, and 5) formed? To address this, we analyzed the electrogenerated chemical species produced during electrosynthesis beyond the primary organic products. Our analysis confirmed the formation of hypochlorite (ClO^-) and ammonia (NH₃) using standard colorimetric methods (Figures 4a and S8–S11).

To trace their formation and role in the side-product pathways, we performed the same electrolysis in a divided electrochemical cell (Figures 4b and S3). ClO⁻, NH₃, and NO₂⁻ were detected exclusively in the anodic compartment. Notably, the product distribution (Figure 4c) revealed that the cathodic compartment selectively produced the desired product 2 via dehalogenation of 1, while the anodic compartment contained all the deaminated byproducts observed in the undivided system (3, 4, and 5) and showed approximately 20% decomposition. A small amount of product 2 detected in the anodic compartment can be attributed to its gradual permeation through the anion-exchange membrane from the cathodic chamber during the prolonged electrolysis.

To further understand the interplay between the identified organic and inorganic species in the reaction mixture, we conducted a series of control experiments (Figure 4d). First, we tested compounds 2 and 4 as substrates under standard electrolysis conditions (reactions i and ii). For compound 2, deamination led to the formation of product 3, while compound 4 underwent dehalogenation to also yield product 3. These results confirm that both deamination and dehalogenation can proceed concurrently under standard conditions, contributing to the observed loss of selectivity.

For the inorganic species, ClO^- is generated as a byproduct of electrochemical chlorine evolution at the anode (Figure S13). Reacting 1 with household bleach (containing 4 to 6% ClO^- content) for 1 h led to 31% degradation of 1, with 25% of the nitrogen atoms from the consumed 1 converted into NH₃ (reaction iii, Figure S12). Furthermore, electrolysis of a 0.5 M NH₃ aqueous solution resulted in the formation of NO₂⁻ (Figure S14). NO₂⁻ is known to react with primary

aromatic amines under strongly acidic conditions to form diazonium intermediates, leading to deamination.³⁸⁻⁴⁰ However, in our system, NO2 does not directly react with compound 1 in the standard highly alkaline electrolyte (reaction iv). A locally acidic environment, generated during electrolysis via water oxidation at the anode, is necessary to promote the deamination process (Figure S36). Taken together, a complete reaction pathway network is established, as shown in Figure 4e. Starting material 1 undergoes dehalogenation to form the desired product 2. However, both 1 and 2 can also undergo deamination to yield sideproducts 3 and 4 via diazonium intermediates, enabled by the presence of NO₂⁻ and the locally acidic environment near the anode. Compound 4 can further dehalogenate to form 3 or undergo decarboxylation to generate 5. The shift in selectivity from 2 toward the formation of side-products 3, 4, and 5 over time is attributed not only to the structural and catalytic evolution of the Ag catalyst, as discussed in Figures 2 and 3 but also to the accumulation of $\mathrm{NO_2}^-$ and H^+ under industrial electrolysis conditions.

Selective and Continuous Synthesis of Aminopyralid by AC Electrolysis. Based on the mechanistic insights above, we propose using AC electrolysis to address the selectivity issues in the electrosynthesis of **2**. AC electrolysis has recently been demonstrated as a promising method for controlling reaction selectivity. Here, the central hypothesis is that continuously alternating the voltage bias facilitates regeneration of defective Ag, the active catalytic structure, thereby preventing electrode deactivation and sustaining high catalytic activity over extended reaction time (Figure 5a). In addition, to suppress the undesired formation of ClO⁻ and the consequent NO_2^- formation, we changed the electrolyte solution from 2% NaOH and 1% NaCl to 2% NaOH in water. Details about the AC electrolysis setup are provided in Figure S2.

Figure 5c presents the conversion of 1 and the yield of 2 after 16 h of AC electrolysis using a square waveform at a fixed amplitude of 1.8 V and frequencies ranging from 1 to 50 mHz. Across all AC conditions, 2 consistently emerged as the dominant product. Optimal performance was observed at 5 mHz, achieving a 90.2% conversion of 1 and a 83.3% yield of 2, corresponding to an impressive selectivity of 92.3%. The optimal frequency of 5 mHz was found to correlate with the Ag surface state, exhibiting the highest activity for the electroreduction of 1 (Figure S37). In stark contrast, industrial electrolysis conditions using a constant voltage of -2.3 V in the same electrolyte resulted in no detectable formation of 2. Instead, it produced significant amounts of deaminated side products 3, 4, and 5. Decreasing the amplitude of the AC waveform reduces the conversion of 1, while increasing it beyond 1.8 V significantly lowers the yield of 2 to approximately 20-30% due to extensive starting material and desired product decomposition (Figure 5d). At the optimal amplitude of 1.8 V, the cathodic potential reaches \sim -1.2 to ~-1.35 V versus Ag/AgCl (Figure S38), matching the cathodic potential of -1.55 V versus Ag/AgCl observed under industrial electrolysis conditions. The high selectivity toward 2 is sustained throughout the 16-h reaction under the optimal AC condition of 5 mHz and 1.8 V (Figure 5e).

Furthermore, the Ag electrode retained its catalytic activity toward the reduction of 1 even after 16 h of AC electrolysis, as evidenced by voltammograms recorded in acetonitrile, which closely resemble those obtained with a freshly anodically

activated Ag electrode (Figure 5b). These results underscore the importance of the dynamic potential profile provided by AC electrolysis, which is crucial for maintaining the high catalytic activity of the Ag catalyst and achieving the desired product selectivity.

We further investigated alternative AC waveforms beyond square waves, including sine and triangular waves. Square waves consistently outperformed the other waveforms (Figure S39), likely because sine and triangular waves did not sufficiently activate the electrode surface, leading to incomplete electrode regeneration and diminished catalytic activity.

We further scaled up the synthesis of 2 using a flow cell system equipped with two Ag plate electrodes (Figure S4). The reaction solution was continuously circulated through the cell until the reaction was complete. Each batch was conducted on a 1 g scale with an initial [1] of 42 mM. Upon completion of a batch, the reaction mixture was replaced with a fresh solution of 1, without removing or reactivating the Ag electrodes. Over the course of 12 consecutive 1 g scale reactions spanning >50 days, all batches consistently showed high conversion of 1 and an average yield of ~85% for 2 (Figure 5f). This result clearly demonstrates that our AC electrolysis protocol enables highly selective and continuous electrosynthesis of 2 without the need for intermittent electrode maintenance, significantly enhancing cost efficiency and operational simplicity—key advantages for industrial applications. 45,46 Following the completion of all batches, the product was isolated by ethyl acetate extraction using a straightforward workup procedure (Figure S5). The final product, obtained as an off-white solid, weighed 7.72 g, corresponding to an isolated yield of 75.2% (Figure 5g). Product purity was confirmed by both ¹H and , ¹³C Nuclear Magnetic Resonance with no detectable impurities (Figures S40 and S41).47

To further demonstrate the generality of our method, we extended it to the electrochemical dehalogenation of 4, producing 3, which is also a widely used commercial herbicide. Under the optimized AC conditions (amplitude: 1.8 V, frequency: 5 mHz, square wave), the reaction afforded 3 in 74.9% yield with 96.4% conversion (Figure S42). In comparison, the industrial method (anodic activation at +2.3 V for 300 s followed by -2.3 V) achieved only a 17.8% yield with 42.7% conversion. These results highlight the advantages of regular electrode reactivation via AC pulses. This marked improvement not only underscores the efficiency of our approach but also demonstrates its potential for direct application to other halogenated precursors, thereby enabling the sustainable synthesis of a broad range of industrially relevant agrochemicals.

Mechanism behind AC-Enabled Selective Synthesis of Aminopyralid. In addition, we analyzed the in situgenerated inorganic species, including ClO^- , NH_3 , and NO_2^- . We found that the AC electrolysis solution contained lower concentrations of all these species compared to the industrial electrolysis conditions: $[\text{NO}_2^-] = 3.2 \text{ vs } 22.3 \text{ ppm}$; $[\text{NH}_3/\text{NH}_4^+] = 42.4 \text{ vs } 169.9 \text{ ppm}$; and $[\text{ClO}^-] = 75 \text{ vs } 100 \text{ ppm}$ (Figure S11). The low NO_2^- concentration under AC conditions is consistent with the minimal formation of deamination side products. To further confirm this, we added NO_2^- to the AC electrolysis reaction. We observed a marked decrease in selectivity, accompanied by the formation of deaminated byproducts 3 and 4 (Figure S15), reinforcing the role of NO_2^- as a key driver of deamination.

The suppressed formation of NO₂⁻ under AC electrolysis conditions arises not only from the lower NH3 concentration in the reaction mixture but also from the reduced anodic potential. CV study indicates that NH3 oxidation on Ag occurs at potentials >1.0 V (Figure S35), higher than the electrode potential of $\sim 0.6~V$ at the anodic pulse 48,49 At anodic potentials below this threshold, only Ag is oxidized, primarily forming Ag(I) species such as Ag₂O.⁴⁹ A small amount of Ag(I) is released into solution, as evidenced by \sim 200 ppm of Ag detected in the reaction mixture after AC electrolysis. Upon polarity reversal in the AC cycle, Ag₂O is reduced back to metallic Ag, regenerating the catalytically active surface, while some dissolved Ag(I) species can also redeposit at the cathode. This dynamic redox cycling helps suppress NO₂⁻ formation and maintains a defect-rich silver surface, which is essential for selective catalysis.

To further investigate the effect of homogeneous Ag(I) species on the catalytic activity, we performed a control reaction by adding $10 \text{ mol } \% \text{ AgNO}_3$ to the reaction mixture and carrying out the process under AC electrolysis conditions. We observed no significant change in the catalytic activity, as most of the dissolved Ag(I) species immediately precipitated as Ag_2O due to the highly basic electrolyte used in this reaction. Therefore, dissolved Ag(I) species have no substantial influence on the reaction.

The overall reaction mechanism behind the AC-enabled selective synthesis of 2 is summarized in Figure 5h. The AC electrolysis system, in combination with a modified Cl $^-$ free electrolyte, effectively suppresses side reaction pathways (highlighted in red) while promoting the desired dehalogenation route (highlighted in green) through three key features: (i) alternating redox pulses enable in situ regeneration of catalytically active Ag defect sites, sustaining dehalogenation reactivity over time; (ii) the removal of NaCl from the electrolyte minimizes the initial formation of ClO $^-$ and prevents undesired oxidative decomposition of the starting material 1 to NH $_3$; and (iii) the redox cycling of Ag between Ag(0) and Ag(I) during AC electrolysis significantly suppresses NH $_3$ oxidation to NO $_2^-$, thereby reducing deamination side reactions.

CONCLUSIONS

In this work, we addressed the long-standing challenge of poor product selectivity in the industrial electrosynthesis of aminopyralid via the dehalogenation of picloram. We identified the root causes of inefficiency in the current industrial process, revealing that catalytically active, defect-rich Ag is responsible for selective dechlorination. However, during prolonged electrolysis, this active Ag structure undergoes reconstruction, while reactive species such as ClO-, NH3, and NO2- are generated in situ, leading to catalyst deactivation and diminished product selectivity. By implementing AC electrolysis, we sustained the active Ag surface and effectively suppressed NO₂⁻ formation, which is responsible for the undesired deamination side reactions. This approach significantly improved product yield, from less than 30% under the current patented industrial method to approximately 85%. We demonstrated the selective and continuous electrosynthesis of aminopyralid for over 50 days at laboratory scale, consistently maintaining high yields. This study not only shows the potential of AC electrolysis to overcome key limitations in aminopyralid production but also establishes it as a generalizable platform for mitigating catalyst degradation and

enhancing selectivity through dynamic control of catalyst structure and reactive species.

ASSOCIATED CONTENT

Solution Supporting Information

The Supporting Information is available free of charge at https://pubs.acs.org/doi/10.1021/jacs.5c12620.

Experimental and instrumentation details, structural analysis of Ag catalyst, details of computational study, CV study in aqueous solution, potential vs time plot for AC electrolysis, and NMR study of aminopyralid (PDF)

AUTHOR INFORMATION

Corresponding Authors

Long Luo — Department of Chemistry, University of Utah, Salt Lake City, Utah 84112, United States; orcid.org/0000-0001-5771-6892; Email: long.luo@utah.edu

Yue Qi — School of Engineering, Brown University, Providence, Rhode Island 02912, United States; ⊚ orcid.org/0000-0001-5331-1193; Email: yueqi@brown.edu

Matthew Neurock — Department of Chemical Engineering and Materials Science, University of Minnesota, Minneapolis, Minnesota 55455, United States; orcid.org/0000-0003-1458-7837; Email: mneurock@umn.edu

Yao Yang — Department of Chemistry and Chemical Biology, Cornell University, Ithaca, New York 14853, United States; orcid.org/0000-0003-0321-3792; Email: yaoyang@cornell.edu

Authors

Diptangshu Datta Mal — Department of Chemistry, University of Utah, Salt Lake City, Utah 84112, United States; orcid.org/0000-0001-7584-8848

Nikita Redkar – School of Engineering, Brown University, Providence, Rhode Island 02912, United States

Kaida Liu – Department of Chemical Engineering and Materials Science, University of Minnesota, Minneapolis, Minnesota 55455, United States

Hyoju Park – Pacific Northwest National Laboratory, Richland, Washington 99354, United States

Ellis Rae Kennedy – Department of Chemistry and Chemical Biology, Cornell University, Ithaca, New York 14853, United States

Sungin Kim — Department of Chemistry and Chemical Biology, Cornell University, Ithaca, New York 14853, United States; ⊚ orcid.org/0000-0001-9107-0781

Wenqi Li – Department of Chemistry and Chemical Biology, Cornell University, Ithaca, New York 14853, United States

Complete contact information is available at: https://pubs.acs.org/10.1021/jacs.5c12620

Author Contributions

All authors have given approval to the final version of the manuscript.

Notes

The authors declare the following competing financial interest(s): A U.S. provisional patent application (No. 63/765,826) based on the technology described in this work was filed on March 4th, 2025, by L.L. and D.D.M. at the University of Utah.

ACKNOWLEDGMENTS

This work is supported by the NSF Center for Synthetic Organic Electrochemistry, CHE-2002158, the University of Utah, and the Alfred P. Sloan Foundation (Grant #FH-2023-20829). H.P. acknowledges support from the U.S. Department of Energy (DOE), Office of Science, Office of Basic Energy Sciences (BES): Material Sciences and Engineering Division, Synthesis and Processing Science Program, FWP 78705, for the high-resolution TEM measurements. This work also made use of Nanofab EMSAL shared facilities of the Micron Technology Foundation Inc. Microscopy Suite, sponsored by the John and Marcia Price College of Engineering, Health Sciences Center, and the Office of the Vice President for Research. E.R.K. is supported by the Eric and Wendy Schmidt AI in Science Postdoctoral Fellowship at Cornell University, a program of Schmidt Sciences, LLC. This work was supported by the Cornell Atkinson Center for Sustainability and the Kavli Institute at Cornell (KIC) Instrumentation Grant. This work made use of TEM facilities at the Cornell Center for Materials Research (CCMR), which are supported through the National Science Foundation Materials Research Science and Engineering Center (NSF MRSEC) program (DMR-1719875). ChatGPT was used to improve the language and clarity of the manuscript during its preparation.

REFERENCES

- (1) Zhao, Z.; Yao, X.; Zhang, L.; Yu, R.; Xu, Y.; Chu, Y.; Mao, X.; Zheng, H. Electrocatalytic dehalogenation in the applications of organic synthesis and environmental degradation. *EcoEnergy* **2024**, 2 (1), 83–113.
- (2) Gerundt, K.; Lewandowski, J.; Putschew, A. Abiotic reductive dehalogenation of pharmaceuticals with naturally occurring redox mediators. *Environ. Adv.* **2025**, *19*, 100622.
- (3) Yao, W.; Liu, T.; Zheng, J.; Yan, S.; Chen, B.; Zhu, X. Cathodic membrane with confined interlayer spacing for efficient electrocatalytic dehalogenation of antibiotics. *J. Membr. Sci.* **2024**, 694, 122417.
- (4) Dutta, N.; Usman, M.; Ashraf, M. A.; Luo, G.; Zhang, S. Efficacy of emerging technologies in addressing reductive dechlorination for environmental bioremediation: A review. *J. Hazard. Mater. Lett.* **2022**, *3*, 100065.
- (5) Sun, G. Q.; Yu, P.; Zhang, W.; Zhang, W.; Wang, Y.; Liao, L. L.; Zhang, Z.; Li, L.; Lu, Z.; Yu, D. G.; et al. Electrochemical reactor dictates site selectivity in N-heteroarene carboxylations. *Nature* **2023**, 615 (7950), 67–72.
- (6) Zhao, Z.; Zhang, R.; Liu, Y.; Zhu, Z.; Wang, Q.; Qiu, Y. Electrochemical C-H deuteration of pyridine derivatives with D_2O . *Nat. Commun.* **2024**, *15* (1), 3832.
- (7) Li, P.; Guo, C.; Wang, S.; Ma, D.; Feng, T.; Wang, Y.; Qiu, Y. Facile and general electrochemical deuteration of unactivated alkyl halides. *Nat. Commun.* **2022**, *13* (1), 3774.
- (8) McDowell, R. D. Process for producing vinyl chloride; US 3,122,591 A, 1964.
- (9) Global Market Insights, Inc. Vinyl Chloride Monomer (VCM) Market; Global Market Insights; Global Market Insights Inc.: Newport Beach, CA, 2024. https://www.gminsights.com/industry-analysis/vinyl-chloride-monomer-vcm-market. (Accessed 26/06/2025).
- (10) Herraiz, I. Chemical Pathways of Corticosteroids, Industrial Synthesis from Sapogenins. *Methods Mol. Biol.* **2017**, *1645*, 15–27.
- (11) Pan, H.; Chang, S.; Qu, Y.; Liu, M.; Tian, W.; Chang, Z. Hydrocortisone production using whole-cell biocatalysts in recombinant Escherichia coli. *Biochem. Eng. J.* **2023**, 198, 109023.
- (12) Verified Market Reports, 2,4-Dichlorophenoxyacetic Acid Market; Verified Market Reports, 2024. https://www.verifiedmarketreports.com/product/2-4-dichlorophenoxyacetic-acid-market/ (Accessed 26/06/2025).

- (13) Verified Market Reports, *Clopyralid Market*; Verified Market Reports, 2024. https://www.verifiedmarketreports.com/product/clopyralid-market/. (Accessed 26/06/2025).
- (14) Song, G.; Wu, H.; Jing, J.; Zhang, X.; Wang, X.; Li, S.; Zhou, M. Insights into Electrochemical Dehalogenation by Non-Noble Metal Single-Atom Cobalt with High Efficiency and Low Energy Consumption. *Environ. Sci. Technol.* **2023**, *57* (38), 14482–14492.
- (15) Im, J.; Mack, E. E.; Seger, E. S.; Loffler, F. E. Biotic and Abiotic Dehalogenation of 1,1,2-Trichloro-1,2,2-trifluoroethane (CFC-113): Implications for Bacterial Detoxification of Chlorinated Ethenes. *Environ. Sci. Technol.* **2019**, *53* (20), 11941–11948.
- (16) Li, L.; Cheng, M.; Ma, C. F.; Yu, W. J.; Jin, J. M.; Wang, J. X.; Liu, W. C.; Lu, C. S.; Zhang, J. J.; Li, X. N. Construction of acid functions and defective sites on carbon supported Ni for HCFC-124 hydrodehalogenation. *Mol. Catal.* 2025, 574, 114858.
- (17) Moreno, J. M.; Aramendía, M. A.; Marinas, A.; Marinas, J. M.; Urbano, F. J. Individual and competitive liquid-phase hydrodechlorination of chlorinated pyridines over alkali-modified Pd/ZrO₂. Appl. Catal., B **2007**, 76 (1–2), 34–41.
- (18) Al-Janabi, N.; Deng, H.; Borges, J.; Liu, X.; Garforth, A.; Siperstein, F. R.; Fan, X. A Facile Post-Synthetic Modification Method To Improve Hydrothermal Stability and CO₂ Selectivity of CuBTC Metal—Organic Framework. *Ind. Eng. Chem. Res.* **2016**, 55 (29), 7941—7949.
- (19) Jeschke, P.; Witschel, M.; Krämer, W.; Schirmer, U. Eds.; New Auxin Mimics and Herbicides *Modern Crop Protection Compounds*; Wiley-VCH, 2019; Vol. 3; pp. 303–350.
- (20) Fast, B. J.; Ferrell, J. A.; MacDonald, G. E.; Krutz, L. J.; Kline, W. N. Picloram and Aminopyralid Sorption to Soil and Clay Minerals. *Weed Sci.* **2010**, 58 (4), 484–489.
- (21) U.S. Geological Survey Estimated Annual Agricultural Pesticide Use: Aminopyralid, 2019. In *Pesticide Use Maps (National Water-Quality Assessment Project)*; U.S. Geological Survey, 2024.
- (22) Verified Market Reports, Amino Acid Herbicide Market; Verified Market Reports, 2024. https://www.verifiedmarketreports.com/product/amino-acid-herbicide-market/. (Accessed 26/06/2025).
- (23) Wang, C.; Scortichini, C. L.; Bridson, T. S. Improved Electrochemical Reduction of Halogenated 4-Aminopicolinic Acids; WO 2,008,042,429 A1, 2008.
- (24) Krumel, K. L.; Bott, C. J.; Gullo, M. F.; Scortichini, C. J.; Hull, J. W., Jr. Electrochemical reduction of halogenated 4-aminopicolinic acids. US 6,352,635 B2, 2010.
- (25) Peerlings, M. L. J.; Han, K.; Longo, A.; Helfferich, K. H.; Ghiasi, M.; de Jongh, P. E.; Ngene, P. Synthesis and Catalytic Performance of Bimetallic Oxide-Derived CuO-ZnO Electrocatalysts for CO₂ Reduction. ACS Catal. 2024, 14 (14), 10701–10711.
- (26) Chen, C.; Yan, X.; Wu, Y.; Liu, S.; Sun, X.; Zhu, Q.; Feng, R.; Wu, T.; Qian, Q.; Liu, H.; et al. The in situ study of surface species and structures of oxide-derived copper catalysts for electrochemical CO₂ reduction. *Chem. Sci.* **2021**, *12* (16), 5938–5943.
- (27) Giziński, D.; Brudzisz, A.; Santos, J. S.; Trivinho-Strixino, F.; Stępniowski, W. J.; Czujko, T. Nanostructured Anodic Copper Oxides as Catalysts in Electrochemical and Photoelectrochemical Reactions. *Catalysts* **2020**, *10* (11), 1338.
- (28) Ophus, C. Four-Dimensional Scanning Transmission Electron Microscopy (4D-STEM): From Scanning Nanodiffraction to Ptychography and Beyond. *Microsc. Microanal.* **2019**, 25 (3), 563–582.
- (29) Kim, S.; Briega-Martos, V.; Liu, S.; Je, K.; Shi, C.; Stephens, K. M.; Zeltmann, S. E.; Zhang, Z.; Guzman-Soriano, R.; Li, W.; et al. Operando Heating and Cooling Electrochemical 4D-STEM Probing Nanoscale Dynamics at Solid–Liquid Interfaces. *J. Am. Chem. Soc.* 2025, 147 (27), 23654–23671.
- (30) Tate, M. W.; Purohit, P.; Chamberlain, D.; Nguyen, K. X.; Hovden, R.; Chang, C. S.; Deb, P.; Turgut, E.; Heron, J. T.; Schlom, D. G.; et al. High Dynamic Range Pixel Array Detector for Scanning Transmission Electron Microscopy. *Microsc. Microanal.* **2016**, 22 (1), 237–249.

- (31) Firet, N. J.; Blommaert, M. A.; Burdyny, T.; Venugopal, A.; Bohra, D.; Longo, A.; Smith, W. A. EXAFS study reveals presence of oxygen in oxide-derived silver catalysts for electrochemical CO reduction. *J. Mater. Chem. A* **2019**, *7* (6), 2597–2607.
- (32) Yang, M.; Wu, J.; Li, Y.; Pan, H.; Cui, H.; Lu, X.; Tang, X. Structural Evolution of Oxide-Derived Nanostructured Silver Electrocatalysts during CO₂ Electroreduction. *ACS Catal.* **2024**, *14* (8), 6169–6178.
- (33) Mattarozzi, F.; van der Willige, N.; Gulino, V.; Keijzer, C.; van de Poll, R. C. J.; Hensen, E. J. M.; Ngene, P.; de Jongh, P. E. Oxidederived Silver Nanowires for CO_2 Electrocatalytic Reduction to CO. ChemCatchem 2023, 15, No. e202300792.
- (34) van Hoof, A. J. F.; Filot, I. A. W.; Friedrich, H.; Hensen, E. J. M. Reversible Restructuring of Silver Particles during Ethylene Epoxidation. *ACS Catal.* **2018**, *8* (12), 11794–11800.
- (35) Irandoust, M.; Shariati-Rad, M.; Haghighi, M. Nitrite determination in water samples based on a modified Griess reaction and central composite design. *Anal. Methods* **2013**, *5* (21), 5977.
- (36) Patton, C. J.; Crouch, S. R. Spectrophotometric and kinetics investigation of the Berthelot reaction for the determination of ammonia. *Anal. Chem.* **1977**, *49* (3), 464–469.
- (37) Guo, Y.; Ma, Q.; Cao, F.; Zhao, Q.; Ji, X. Colorimetric detection of hypochlorite in tap water based on the oxidation of 3,3′,5,5′-tetramethyl benzidine. *Anal. Methods* **2015**, 7 (10), 4055–4058.
- (38) Berger, K. J.; Driscoll, J. L.; Yuan, M.; Dherange, B. D.; Gutierrez, O.; Levin, M. D. Direct Deamination of Primary Amines via Isodiazene Intermediates. *J. Am. Chem. Soc.* **2021**, *143* (42), 17366–17373.
- (39) Si, T.; Cho, H.; Kim, H. Y.; Oh, K. ortho-Naphthoquinone-Catalyzed Aerobic Hydrodeamination of Aryl Amines via in Situ Dediazotization of Aryl Diazonium Species. *Org. Lett.* **2022**, *24* (46), 8531–8535.
- (40) Mateos, J.; Schulte, T.; Behera, D.; Leutzsch, M.; Altun, A.; Sato, T.; Waldbach, F.; Schnegg, A.; Neese, F.; Ritter, T. Nitrate reduction enables safer aryldiazonium chemistry. *Science* **2024**, 384 (6694), 446–452.
- (41) Behera, N.; Rodrigo, S.; Hazra, A.; Maity, R.; Luo, L. Revisiting Alternating Current Electrolysis for Organic Synthesis. *Curr. Opin. Electrochem.* **2024**, 43, 101439.
- (42) Rodrigo, S.; Hazra, A.; Mahajan, J. P.; Nguyen, H. M.; Luo, L. Overcoming the Potential Window-Limited Functional Group Compatibility by Alternating Current Electrolysis. *J. Am. Chem. Soc.* **2023**, *145* (40), 21851–21859.
- (43) Hayashi, K.; Griffin, J.; Harper, K. C.; Kawamata, Y.; Baran, P. S. Chemoselective (Hetero)Arene Electroreduction Enabled by Rapid Alternating Polarity. *J. Am. Chem. Soc.* **2022**, *144* (13), 5762–5768.
- (44) Kawamata, Y.; Hayashi, K.; Carlson, E.; Shaji, S.; Waldmann, D.; Simmons, B. J.; Edwards, J. T.; Zapf, C. W.; Saito, M.; Baran, P. S. Chemoselective Electrosynthesis Using Rapid Alternating Polarity. *J. Am. Chem. Soc.* **2021**, *143* (40), 16580–16588.
- (45) Hessel, V.; Mukherjee, S.; Mitra, S.; Goswami, A.; Tran, N. N.; Ferlin, F.; Vaccaro, L.; Galogahi, F. M.; Nguyen, N.-T.; Escribà-Gelonch, M. Sustainability of flow chemistry and microreaction technology. *Green Chem.* **2024**, *26* (18), 9503–9528.
- (46) Ramírez-Márquez, C.; Al-Thubaiti, M. M.; Martín, M.; El-Halwagi, M. M.; Ponce-Ortega, J. M. Processes Intensification for Sustainability: Prospects and Opportunities. *Ind. Eng. Chem. Res.* **2023**, *62* (6), 2428–2443.
- (47) ChemicalBook Spectrum of AMINOPYRALID(150114-71-9) ¹H NMR; ChemicalBook, 2025.
- (48) Sugianto Prabowo Rahardjo, S.; Shih, Y.-J. In-situ phase transformation of silver oxide nanoparticles encapsulated in reduced graphene oxide (Ag/rGO) for direct electrochemical ammonia oxidation. *Chem. Eng. J.* **2023**, 473, 145396.
- (49) Vu, T. M.; Johnston, S.; Simondson, D.; Nguyen, C. K.; Nguyen, T. D.; Zeil, D. V.; Hocking, R. K.; Macfarlane, D. R.; Simonov, A. N. High-Rate High-Selectivity Electrochemical Oxidation

of Ammonia to Nitrite with a Silver-Based Catalyst. ACS Catal. 2024, 14 (14), 10974–10986.

